JSAE 20077143
SAND2007-2315C
SAE 2007-01-1837

On the Cyclic Variability and Sources of Unburned Hydrocarbon Emissions in Low Temperature Diesel Combustion Systems

Will F. Colban and Paul C. Miles
Combustion Research Facility, Sandia National Laboratories, Livermore, CA, USA

Seungmook Oh
Korea Institute of Machinery and Materials, Daejeon, S. Korea

ABSTRACT

The cycle-to-cycle variability and potential sources of unburned hydrocarbon (UHC) emissions are examined in a single-cylinder, light-duty diesel test engine operating in low-temperature combustion regimes. A fast flame ionization detector (FID) was employed to examine both cycle-to-cycle variations in UHC emissions and intra-cycle emissions behavior. A standard suite of emissions measurements, including CO, CO_2, NO_x, and soot, was also obtained. Measurements were made spanning a broad range of intake O_2 concentrations—to examine the UHC behavior of dilution-controlled combustion regimes—and spanning a broad range of injection timings—to clarify the behavior of increased UHC emissions in late-injection combustion regimes. Both low- and moderate-loads were investigated.

The cycle-resolved UHC data showed that the coefficient of variation of single-cycle UHC did not increase with increases in UHC emissions as either O_2 concentration or injection timing was varied. Increases in UHC emissions thus result from deterioration in the performance of the mean (or typical) cycle, not from increasing single-cycle variation. Additionally, the crank-angle-resolved UHC measurements were coupled with a 1-D engine model to examine the variation of exhaust mass flow rate of UHC within each cycle. The results showed that most of the UHC mass exited the cylinder during the latter part of the exhaust process, and that UHCs originating from cylinder wall and piston top quench layers are likely of greater importance than UHCs emitted from quench layers along the head.

INTRODUCTION

Unburned hydrocarbon (UHC) emissions from direct-injection (DI) diesel engines have been traditionally considered to be of secondary importance as compared to the emissions of soot and NO_x, due to the high combustion efficiency of these engines and the diminished importance of combustion chamber crevices as a potential source. Low temperature combustion (LTC) strategies employed to simultaneously lower NO_x and particulate emissions, however, not only reduce these pollutants to manageable levels but also result in elevated UHC (and CO) emissions. Hence an understanding of the sources of these emissions is now needed to enable optimal development of diesel LTC systems.

As discussed in Heywood [1], there are a number of possible sources of UHC emissions in DI diesel engines. First, overmixing of fuel to local equivalence ratios below the lean combustion limit forms regions which do not permit complete combustion on relevant engine time scales. Overmixing is thought to occur at low loads, particularly for conditions where the ignition delay is long and allows for a long mixing time. Similarly, undermixing can also occur whereby locally rich regions are created which also do not support complete combustion. Undermixing is generally thought to occur as a result of over fueling or when vaporized fuel from the injector sac volume exits into the cylinder during expansion. Another source of UHC includes wall quenching of fuel-air mixture coming into contact with cool surface boundary layers on the firedeck and piston top. Fuel can also become trapped in crevice volumes and outgased as UHC during the exhaust stroke. A final source of UHC results from late-cycle bulk gas quenching of incomplete combustion products, whereby the slower mixing-limited combustion ceases because of falling in-cylinder temperatures.

Fast flame ionization detectors (FID) have been used previously to get time-resolved measurements of UHC both in-cylinder and in the exhaust port. However, previous UHC fast-FID work has mainly focused on spark ignition (SI) gasoline engines. Finlay et al. [2] used a fast-FID probe placed at various locations downstream of the exhaust valve stem in the exhaust port of a SI engine to show the importance of FID probe location within the exhaust port. The FID signal maintained roughly the same profile for up to 30 mm downstream of the exhaust

valve stem, before mixing within the exhaust port distorted the signal from its original shape.

Another study using a fast-FID in the exhaust port of an SI engine, carried out by Jensen et al. [3], coupled time-resolved fast-FID UHC sampling with predicted exhaust mass flow rates to obtain single-cycle mass-averaged UHC emissions. They compared their mass-averaged UHC emissions with average UHC measurements taken with a traditional FID system and found good agreement.

In SI work done by Tabaczynski et al. [4], a fast sampling valve rather than a fast-FID was used to obtain UHC concentration measurements with a temporal resolution on the order of 2 ms. Simultaneously, the instantaneous exhaust mass flow rate was also measured using an orifice plate in the exhaust manifold. Their analysis showed that roughly 40% of UHC mass exited during the blowdown. They attributed the blowdown UHC emissions to quenched gases on the head surface (firedeck). They also found that approximately 50% of the UHC mass was accounted for near the end of the exhaust stroke, caused by a hydrocarbon-rich vortex which lifted quenched UHC off the cylinder liner.

Fast-FID measurements in an SI engine were done by Marriott et al. [5], in which their instantaneous measurements were combined with predicted exhaust gas mass flow rates to determine the mass flow rate of UHC during the exhaust event. They also reported that a significant portion of the UHC seen during the blowdown event could be from quenched gases near the exhaust valve and cylinder head, and reported that the contribution from quenched gas near the firedeck increased with load.

There has not been a significant amount of work done with fast-FID detection of UHC in the exhaust port of DI diesel engines. The study by Schurov et al. [6] presents fast-FID traces of UHC taken in the exhaust port of a diesel engine, although there is no further analysis done with the data to try to examine the sources of UHC based on exhaust mass flow rate. The continuously fired data of Schurov et al. [6] shows a slight increase in UHC level at exhaust valve opening (EVO), likely resulting from the purging of quenched gases near the firedeck. The UHC concentration then falls as the bulk gases dominate the next period of exhaust. Finally, just prior to exhaust valve closing (EVC), UHC levels increased again, indicating possible expulsion of residual UHC from a combination of crevice sources and quenched gases on the cylinder walls. The UHC level in the exhaust port remained high until the next EVO.

In the current study, similar to previous studies performed in SI engines, our objective is to employ the fast-FID measurements to examine the dominant sources of UHCs within the cylinder. By coupling time-resolved UHC concentration obtained with the fast-FID to numerical exhaust mass flow rate predictions, a greater understanding of the sources of UHC and their relative importance can be achieved. In addition, we seek to examine the nature of the cycle-to-cycle variations in UHCs with the objective of determining the level of complexity that must be included into engine simulation models in order to capture the behavior of UHC emissions.

EXPERIMENT

RESEARCH ENGINE

The research engine is based on a General Motors 4-cylinder 1.9 liter production engine, modified to operate as an optically-accessible single-cylinder test engine. The head is equipped with 4 valves canted approximately 2° from vertical and a central, vertical Bosch CRIP 2.2 injector. The production glow plug has been removed and the hole modified to accept a Kistler 6125B piezoelectric pressure transducer, mounted such that its face is recessed approximately 5.6 mm from the firedeck. The main geometrical characteristics of the engine and fuel injection system, including a dimensionally accurate representation of the bowl geometry, are given in Figure 1 and Table 1.

Because the engine is designed to facilitate optically-based measurements, it has certain features which distinguish it from a conventional all-metal test engine. Foremost among these features is the oversize top ring-land crevice. The top ring-land is characterized by a height of 30.9 mm and a width of 0.18 mm, giving a total volume of 1.4 cc—nearly 5% of the

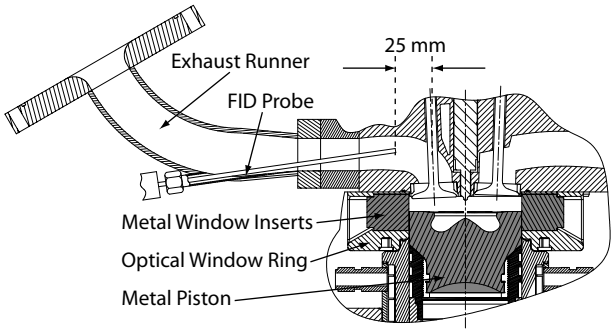

Figure 1. Schematic of the engine showing the location of the fast-FID probe. The piston bowl geometry shown is a faithful representation of the actual bowl shape.

Table 1. Engine Specifications

Basic Geometry	
Bore:	82.0 [mm]
Stroke:	90.4 [mm]
Displacement Volume:	477 [cm^3]
Geometric CR:	16.7
Squish Height:	0.78 [mm]
Swirl Ratio:	2.2

Valve Events (0.15 mm lift)			
IVO:	-359°CA	EVO:	132°CA
IVC:	-152°CA	EVC:	360°CA

Fuel Injector	
Number of Holes:	7
Included Angle:	149°
Sac Volume:	0.12 [mm^3]
Nozzle Hole Diameter:	0.14 [mm]
Flow Number:	440

combined bowl and squish volume (including piston-top valve pockets) of 29.0 cc at top dead center (TDC). This crevice reduces the geometric compression ratio from 17.4 for a conventional ring-land crevice to 16.7 in the current engine setup. A second notable difference is the cylinder wall cooling arrangements—the upper portion of the cylinder liner can be fitted with quartz windows, and is uncooled.

The two intake ports consist of a tangential port that imparts significant swirl motion to the in-cylinder flow and a second "fill" port with a lesser swirl generation capability. The ports can be individually throttled to vary the in-cylinder swirl ratio. For this work, both throttles were fully-open, corresponding to a swirl ratio of approximately 2.2. The ports are fed through short, curved runners with a flow length along the centerline of approximately 23 cm and 24 cm for the intake and exhaust runners, respectively. Plenum chambers with a volume of 80 times the engine displacement provide a constant pressure boundary at the intake runner inlet and exhaust runner exit.

OPERATING CONDITIONS

For the investigations reported here, the engine speed was maintained constant at 1500 RPM and two different engine loads were investigated, a low load of nominally 3 bar IMEP and a higher load of nominally 8 bar IMEP. For any given parameter sweep at fixed load, the fueling rate was held constant.

Although the engine was operated with a metal piston installed, the optically-accessible design did not allow for continuous firing because of over-heating constraints. Consequently, the engine was run skip-fired, with fuel injection occurring on one of every 4 cycles during testing. Prior to skip-firing, the engine was motored for 2 minutes, during which time the intake pressures stabilized and the combustion chamber surfaces experienced some degree of preheating. The engine was then skip-fired for 1 minute to allow the gas composition in the exhaust plenum to reach an approximately steady value, and to allow exhaust gases to reach the emissions analyzers and for the analyzer output to stabilize. At the end of this period, soot sampling and acquisition of cylinder pressure and gaseous emissions data commenced simultaneously. Because the gas composition in the exhaust plenum was still changing slowly during the sampling period, we adhered strictly to the time schedule described above to ensure that these changes affected the measured emissions equally for all data sets. Pressure and emissions were sampled with 0.25°CA resolution for 75 skip-fired cycles (representing 300 total engine cycles). After taking data, the engine was stopped and allowed to cool for 6 minutes before taking another data set. A fixed cooling period ensured that the thermal state of the engine was also identical for all tests.

There were two main investigations in this study. In the first the O_2 concentration at maximum brake torque (MBT) timing was varied and in the second the start-of-injection (SOI) at fixed O_2 concentration was varied. For each investigation, both the 3 and 8 bar loads were tested. The intake plenum pressure was fixed at 1.5 ± 0.05 bar, and the exhaust plenum pressure was typically 1.8 ± 0.1 bar. A constant injection pressure was also maintained at 860 bar.

To obtain the desired O_2 concentration, the engine was run with simulated exhaust gas recirculation (EGR) by adding N_2 and CO_2 to the inlet stream. Water vapor and trace amounts of unburned fuel and other emissions were neglected in the EGR composition for this study. The relative proportions of N_2 and CO_2 were selected to match the specific heat ratio of real engine exhaust gases at 600 K. While the proportions of Air, N_2, and CO_2 were varied depending on the desired O_2 concentration, the total mass flow rate was fixed to maintain a constant TDC density. As intake charge composition varies, however, the charge compression temperature also varies due to the changing mixture specific heat ratio. To eliminate the influence of changing TDC temperature on the emissions behavior observed as O_2 concentration was varied, the intake temperature was also varied to maintain a fixed TDC "core" temperature of 941 K on cycles without fuel injection. The core temperature, characteristic of the temperature away from the combustion chamber surfaces, is expected to be close to the adiabatic compression temperature. The intake temperature required to maintain a fixed core temperature was pre-calculated accounting for the temperature-dependent specific heat ratios of the intake charge component gases. The resultant intake temperatures, as well as the equivalent EGR rates and the corresponding average in-cylinder equivalence ratios for each O_2 concentration are listed in Table 2.

As shown in Figure 2, the IMEP differed somewhat from the nominal value as O_2 concentration was varied, falling off towards lower O_2 concentrations despite the use of fixed fueling. COV levels indicate that higher loads produced more stable operating conditions, and that COV increased somewhat as the load began to drop at low O_2 concentrations.

For the injection timing sweeps a fixed O_2 concentration of 15% was used. The shaded row in Table 2 indicates the conditions for the SOI sweep. Figure 3 shows the variation in IMEP with injection timing. There was a slight drop in IMEP at both very early and very late injection timings, however, overall IMEP levels were fairly constant. Although overall IMEP was quite stable, COV levels again showed that more variation occurred at low loads.

Table 2. Engine Operating Conditions (the shaded row indicates the conditions for the SOI sweep at 15% O_2)

		3 bar			8 bar		
O_2 [%]	T_{in} [°C]	SOI [°CA]	EGR [%]	ϕ_{avg} [-]	SOI [°CA]	EGR [%]	ϕ_{avg} [-]
8	101.8	-29.3	77.8	0.45	-34.7	58.2	1.17
9	97.4	-28.4	76.4	0.40	-32.9	56.2	1.03
10	97.1	-26.6	75.0	0.36	-31.1	54.1	0.93
11	97.0	-22.1	73.3	0.32	-22.1	51.9	0.83
12	93.5	-19.4	71.2	0.29	-17.6	49.4	0.76
13	92.9	-16.7	69.0	0.27	-16.7	46.5	0.70
15	87.2	-13.1	62.7	0.23	-14.0	39.5	0.60
17	84.0	-12.2	52.9	0.20	-12.2	30.3	0.52

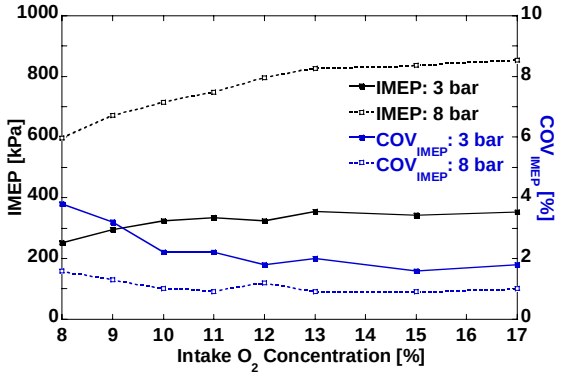

Figure 2. IMEP and COV_{IMEP} variation with O2 concentration at both load conditions.

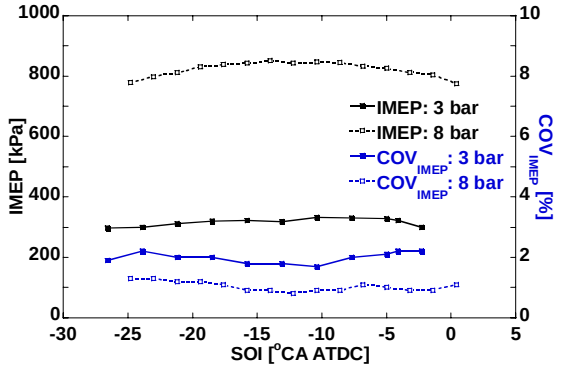

Figure 3. IMEP and COV_{IMEP} variation with SOI at both load conditions.

FID SET-UP AND EMISSIONS EQUIPMENT

The UHC measurements were made using a Cambustion HFR 400 fast flame ionization detector (FID) equipped with a constant pressure system and a heated sampling line. The fast-FID probe was positioned in the exhaust port approximately 25 mm downstream from the exhaust valve stem, as shown in Figure 1. The fast-FID had a response time of roughly 0.5 ms (4.5°CA at 1500 RPM) to changes in HC levels, allowing time-resolved UHC measurements from the exhaust stream. The transit time for the probe—the time required for the sample to travel from the probe tip to the FID—was about 3.5 ms (31.5°CA at 1500 rpm). The fast-FID was dynamically calibrated with span gas (propane at 950 ppm) while the engine was skip-fired to remove any temperature and pressure effects.

Soot concentrations in the exhaust were measured using an AVL 415S smoke meter, which was positioned downstream of the exhaust plenum. A sample of the exhaust gas was drawn through a clean section of filter paper by the smoke meter. The smoke meter then measured the reflectivity of the filter paper, comparing it to the reflectivity value of the clean filter paper measured before the sample to generate the paper blackening number. The sample volume, which was 3.0 L for all cases, was then used to convert the paper blackening number to a filter smoke number (FSN). As noted above, soot sampling was performed at the same time as the gaseous emission measurements.

Emissions of NO_x were taken using a California Instruments 600 Heated Chemiluminescent NO/NO_x Analyzer (HCLD). The range was toggled between 0-30 ppm and 0-300 ppm, depending on the NO_x levels at each operating condition. Exhaust levels of CO and CO_2 were measured with a California Instruments 300 Nondispersive Infrared (NDIR) Gas Analyzer. The range of measurable CO levels was 0-6000 ppm, while CO_2 had a range of 0-15%. Exhaust samples were taken continuously from the exhaust plenum using a heated sampling line. The exhaust was then drawn through a condenser to remove water and condensable hydrocarbons before going to the HCLD and NDIR gas analyzers.

DATA ANALYSIS

PRESSURE

The fired in-cylinder pressure data were used to obtain indicated mean effective pressure (IMEP), apparent heat release (burn) rate (AHRR), and the ignition delay periods, which were then cycle-averaged to give the values reported here. Motored (no fuel injection) in-cylinder pressure data were also taken at each operating condition to assist in the heat release analysis and calculate the burn rate profile. The heat release analysis is performed following an iterative two-zone procedure using temperature and mixture dependent gas properties, as described by Kook et al. [7].

EMISSIONS ANALYSIS

The sampled values of the gaseous emissions were averaged over the last 30 cycles acquired, by which time the drift in the emissions due to mixing in the plenum and the changing thermal state of the engine was minimal. Because the sampled exhaust gases contained a mixture of exhaust from fired and motored cycles, the measured emissions were corrected for dilution with the exhaust gases from motored cycles. A small correction was also applied to the measured (dry) NO_x, CO, and CO_2 mole fractions to account for the residual water vapor in the gases exiting the condenser.

An emissions analysis was performed at each crank angle using the temporally-resolved UHC mole fractions provided by the fast-FID, following an analysis procedure similar to that outlined by Silvis [8]. For the purpose of this analysis, the measured mole fractions of the remaining species were assumed constant for the entire exhaust process. The H- and C-atom balance equations, modified to account for the CO_2 in the intake stream, were combined with the water-gas shift equilibrium relationship (K_{eq} = 3.65) to solve for the wet H_2O mole fraction. Subsequently, the measured dry mole fractions of CO and CO_2 were corrected for the missing water, and used with the water-gas shift relationship to estimate the H_2 mole fraction. The C-atom, N-atom, and O-atom balance equations then provided the number of product gas moles per mole of fuel, the N_2 mole fraction, and the O_2 mole fraction, respectively. A final equation, requiring that the product gas mole fractions sum to

unity, was not employed directly but used to check the measurements for consistency.

The computed wet mole fractions were converted to species mass fractions, and multiplication of the UHC mass fraction by the instantaneous exhaust gas mass flow, computed as described below, yielded the crank-angle resolved UHC mass emissions. To perform cycle-averaged emissions analysis, an appropriate "average" UHC mole fraction is required. This analysis was performed using an average UHC mole fraction that provided the identical average exhaust gas UHC mass fraction obtained by integrating the instantaneous mass flows over the exhaust stroke. Emission indices for each species were then obtained by multiplying the cycle-averaged mass fractions by the average exhaust gas mass flow rate (less the simulated EGR mass flow). The combustion efficiency is then computed from emissions data by the expression given in Heywood [1].

DESCRIPTION OF THE WAVE MODEL

The instantaneous mass flow rate exiting the cylinder during the exhaust stroke is required to convert the UHC concentrations obtained with the FID into a crank-angle resolved record of UHC mass emissions. Ricardo's 1-D finite difference engine simulation code, WAVE v7.1, was used to predict the crank-angle-resolved exhaust mass flow rate for each operating condition. WAVE solves the compressible and time-dependent conservation equations of mass, momentum, and energy within the intake and exhaust runners and the cylinder. Boundary conditions for each operating condition were taken from the experiments. To match the experimental combustion process, the measured burn rate profile from each operating condition was used as an input. Some representative burn rate profiles for different cases are shown in Figures 4 and 5, along with their corresponding pressure traces.

RESULTS AND DISCUSSION

CYCLE AVERAGED EMISSIONS BEHAVIOR

Cycle-averaged emissions for the O_2 sweeps are shown in Figures 6 and 7. The ignition delay, defined here as the time between SOI and the 10% burn angle, is also shown in Figure 6, and was greater than the injection duration for all conditions. As O_2 concentration was reduced, oxidation of HC, CO, and soot was decreased, causing UHC, CO, and soot emissions to increase. Continued decreases in O_2 concentration, however, result in a reduction of soot formation and a leveling off in CO at high load. A characteristic soot 'hump', resulting from a trade-off between falling formation and oxidation rates, is shown clearly in Figure 7 for the 8 bar condition. To a lesser degree, the CO emissions also exhibited this behavior at the 8 bar condition, as evidenced by a leveling off of CO at O_2 concentrations less than 11% in Figure 6. At these low O_2 concentrations the CO concentrations were well within the calibrated range of the emissions analyzer. CO emissions at low O_2

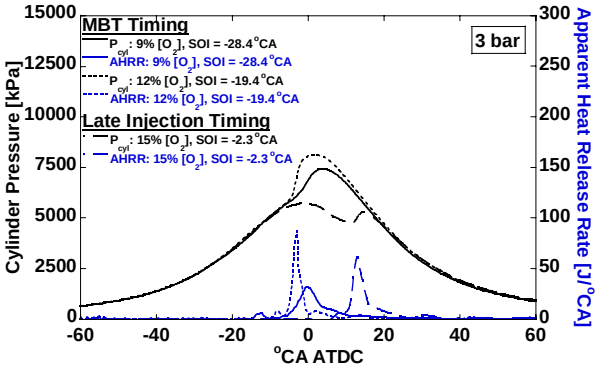

Figure 4. Cylinder pressure traces and burn rate profiles at 3 bar load for MBT timing conditions at 9% and 12 % O_2 and a late injection timing condition.

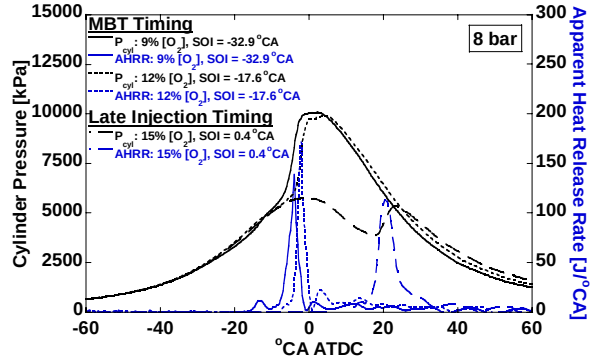

Figure 5. Cylinder pressure traces and burn rate profiles at 8 bar load for MBT timing conditions at 9% and 12 % O_2 and a late injection timing condition.

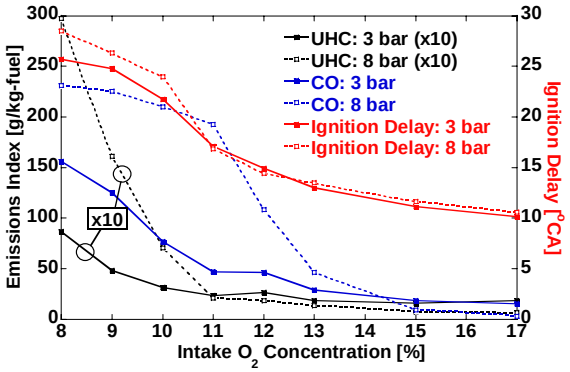

Figure 6. Cycle averaged UHC and CO emissions for a sweep of O_2 concentrations at 3 and 8 bar loads with corresponding ignition delay.

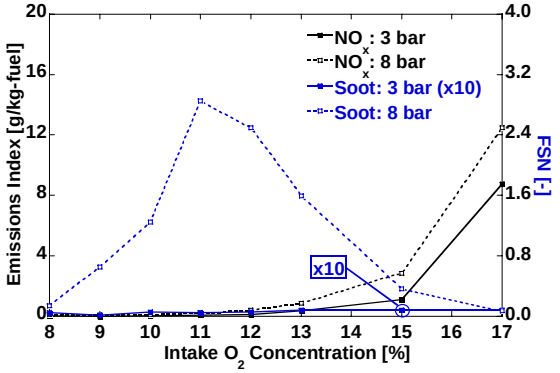

Figure 7. Cycle averaged NO_x and soot emissions for a sweep of O_2 concentrations at 3 and 8 bar loads.

concentrations are typically observed to increase monotonically as O_2 concentration is reduced (e.g. [9], [10], and [11]). However, our study shows CO emissions leveling off somewhat towards lower O_2 concentrations at the 8 bar load.

Greater soot production at the higher load is expected due to the higher probability of locally-rich equivalence ratios associated with the overall richer fuel-air mixture. Increased cylinder pressure also results in increased compressive heating of the in-cylinder gases, and higher peak combustion temperatures—leading to still greater soot production. There is little soot production for the 3 bar load case, as the FSN was extremely low with an average FSN near 0.005 for the range of O_2 concentrations tested (note the resolution of the smokemeter was only 0.001).

NO_x exhibits the expected trends, decreasing with decreasing O_2 concentration to very low levels. At high load, NO_x levels were higher due to higher combustion temperatures.

In general, higher emissions were seen at the higher load, the exception being UHC and CO at O_2 concentrations above 11% and 14%, respectively. This behavior in UHC and CO emissions is mirrored by the combustion efficiency shown in Figure 8. At high O_2 concentrations, combustion efficiency is better at high load than at low load. However, as O_2 concentration is reduced, UHC and CO emissions begin to rise more rapidly at the 8 bar condition and the high load combustion efficiency falls off more than at low load. This behavior suggests that at high O_2 concentrations, the kinetics of oxidation of CO and UHC is a dominant factor influencing the engine-out emissions, rather than mixing with available O_2. At the higher load, higher in-cylinder temperatures increase oxidation rates. Conversely, for those O_2 concentrations at which the low-load CO and UHC emissions (and combustion efficiency) are superior, it is probable that the dominant limiting factor for the high load oxidation process is mixing.

Results of cycle averaged emissions and ignition delay for the SOI sweeps are shown in Figures 9 and 10. Also shown on Figures 9 and 10 are emissions measured at MBT timing conditions with 15% O_2, presented for comparison and to provide a sense of

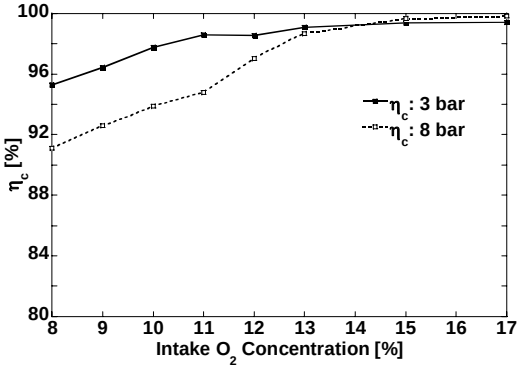

Figure 8. Combustion efficiency at MBT timing for the 3 and 8 bar loads as a function of O_2 concentration.

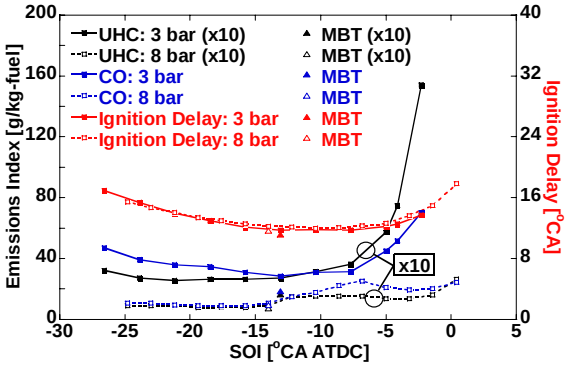

Figure 9. Cycle averaged UHC and CO emissions for a range of SOI at 3 and 8 bar loads with corresponding ignition delay.

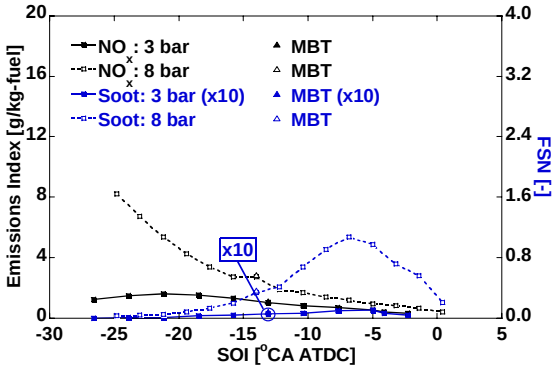

Figure 10. Cycle averaged NO_x and soot emissions for a range of SOI at 3 and 8 bar loads.

measurement repeatability, which overall was quite good. Trends in emissions are similar to those noted by other studies incorporating late-injection timing and high-EGR rates, such as Nissan's MK-type combustion [12]. At late injection timings, a downturn in NO_x and soot corresponds to a rise in both CO and UHC. NO_x emissions generally decrease with retarded SOI as a result of lower combustion temperatures.

As the start of injection was retarded from the most advanced timing, soot initially increased. It is tempting to interpret the increase as due, in part, to decreased mixing associated with the decreased ignition delay. However, it should be recalled that the average ambient gas density is increasing as SOI is retarded, resulting in higher rates of ambient gas entrainment into the fuel jets. Soot levels reached a maximum near SOI = -7°CA, before decreasing again as SOI continued to retard. The latter decrease in soot is likely due to increased mixing associated with the rising ignition delay (at roughly constant or rising ambient density), as well as falling peak combustion temperatures due to cylinder volume expansion during the ignition delay period. The soot 'hump' was observed for both load conditions, although FSN levels are two orders of magnitude lower at the 3 bar load (again note that the FSN values for the 3 bar load are on the order of the resolution of the smoke meter).

The combustion efficiency, shown in Figure 11 for the SOI sweeps, again closely follows the trends in UHC and CO emissions. Combustion efficiency is consistently lower for the 3 bar load at nominally η_c =

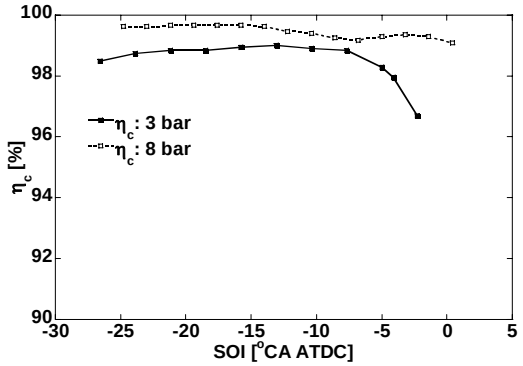

Figure 11. Combustion efficiency as a function of SOI for the 3 and 8 bar loads.

98%, with correspondingly higher UHC and CO emissions. A higher combustion efficiency of η_c = 99% is seen at the 8 bar load, with less drop off at retarded injection timings, corresponding to less turn-up in UHC and CO emissions. As seen previously for the sweeps of O_2 concentration, this behavior suggests that oxidation of CO and UHC at low load is rate-limited by chemical kinetics, rather than mixing.

INTRA-CYCLE UHC BEHAVIOR

Examination of fast-FID traces of UHC

As stated previously, the engine was skip-fired every four cycles, generating useful UHC data only during the fired cycle. The fast-FID traces of UHC concentration in ppm C_3 are shown in Figures 12a-d for each test case, averaged over the 75 skip-fired cycle sequences obtained. Note the difference in scale amongst Figures 12a-d, only Figures 12a and 12b are the same. Each cycle is designated on the figures, as well as the 0.15 mm lift EVO and EVC times. Also shown for the fired cycles are the equivalent EVO and EVC events, accounting for the time delay from when the sample exits the exhaust valve until it is measured by the FID.

The effect of motoring the engine for three cycles between each fired cycle was to sequentially reduce the UHC level in the exhaust port. The concentration of UHC in the exhaust port did not reach zero prior to each fired cycle, as might be expected after dilution by the three intermediate motored cycles. The rather slow decrease in the port concentrations of UHC suggests that a significant amount of UHC is not scavenged effectively from the cylinder during the exhaust period.

One possible explanation for this poor scavenging is the formation of liquid films within the cylinder, which survive through multiple cycles. Such films can be expected to form at the early injection timings employed at the lowest O_2 concentrations. However, very similar scavenging behavior is observed under conditions when no liquid impingement on combustion chamber surfaces is expected (that is, with injection near TDC as seen in Figures 12c and 12d). For that reason, outgassing of liquid films is not believed to be a primary source of the residual UHC levels during the motored cycles.

A second potential source of “apparent” poor scavenging is storage of UHC within the FID probe and sample lines. Such storage might be due to condensed UHC within the sample line, or to UHC adsorbed onto soot deposits. The first storage mechanism seems unlikely, as the sample line was heated to 150°C during the tests. Moreover, similar scavenging behavior is observed at operating conditions with much lower UHC emissions, with little potential for condensation. The sample line was cleaned on a daily basis, and no difference in scavenging behavior was observed in tests conducted shortly after cleaning. Hence, this mechanism also appears improbable.

The most probable explanation for the poor scavenging is backflow of exhaust gases from the port into the cylinder during the exhaust process. During motored cycles, the exhaust plenum pressure is roughly 10-20 kPa higher than the in-cylinder pressure at EVO. This pressure differential causes exhaust backflow into the cylinder equal to approximately 12% of the motored charge by mass. Accounting for this backflow, a residual gas mass fraction of 6% at IVO, and assuming a homogeneous mixture composition (rapid and complete mixing), 30-45% of the residual UHC signal (depending on the operating condition) measured during the first motored cycle can be explained. Although the sources of elevated UHC signals during the motored cycles are only partially known, it is not believed that the residual signal significantly affects the fired-cycle trends or the conclusions of this study.

A close examination of the fast-FID traces provides some insight into the sources of UHC. The fired cycles from the fast-FID traces in Figures 12a-d have been enlarged, and are shown again in Figures 13a-d. The fast-FID traces have also been shifted to account for the time delay between the valve events and the FID response.

As an example interpretation of these Figures, consider the 9% and 10% O_2 concentration cases at 8 bar shown in Figure 13b, in which there was a significant rise in UHC concentration immediately following EVO. Very early injection timings for these two cases (SOI = -32.9°CA for 9% and SOI = -31.1°CA for 10%) suggest that the rapid rise could be caused by fuel trapped in the squish volume and in quench layers along the head and valve surfaces. Following EVO, UHC in these quench layers would be expelled immediately. Figure 14 shows a fuel spray targeting schematic at SOI = -30°CA and SOI = 0°CA, taking into account a 4.6°CA delay between the SOI command and the actual fuel injection event when determining piston position. A fuel spray half angle of roughly 10°, determined from the correlation of Naber and Siebers [13], is also shown in Figure 14. The spray targeting shown for SOI = -30°CA indicates that a substantial amount of fuel enters the squish volume at early SOI timings, and that the spike seen at 9% and 10% O_2 concentrations at 8 bar could be the result. Smaller initial rises in UHC for the 8% and 9% O_2 conditions at 3 bar load (Figure 13a), which also have fairly early injection timings, could also be attributed to the same phenomenon.

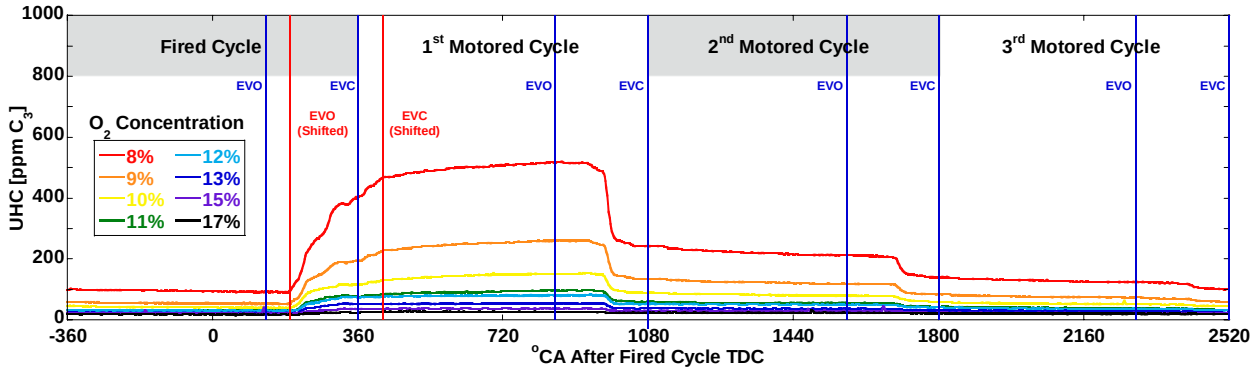

a)

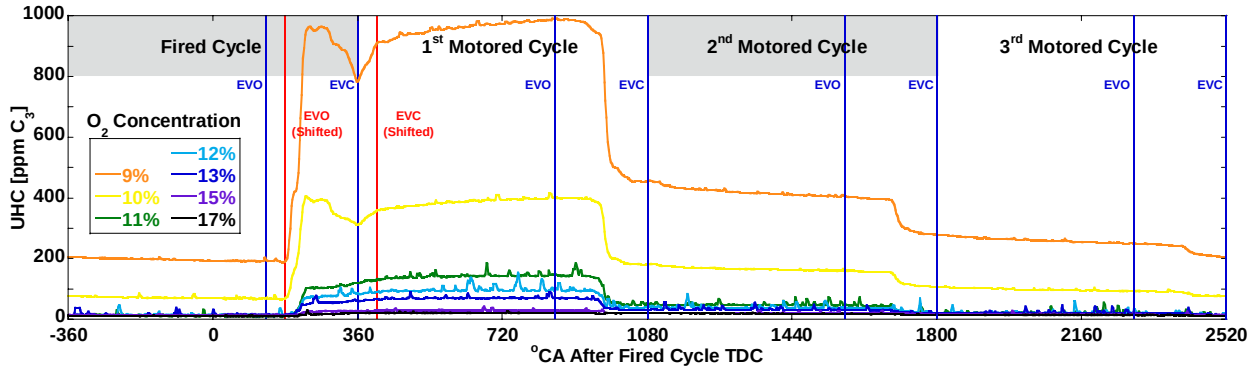

b)

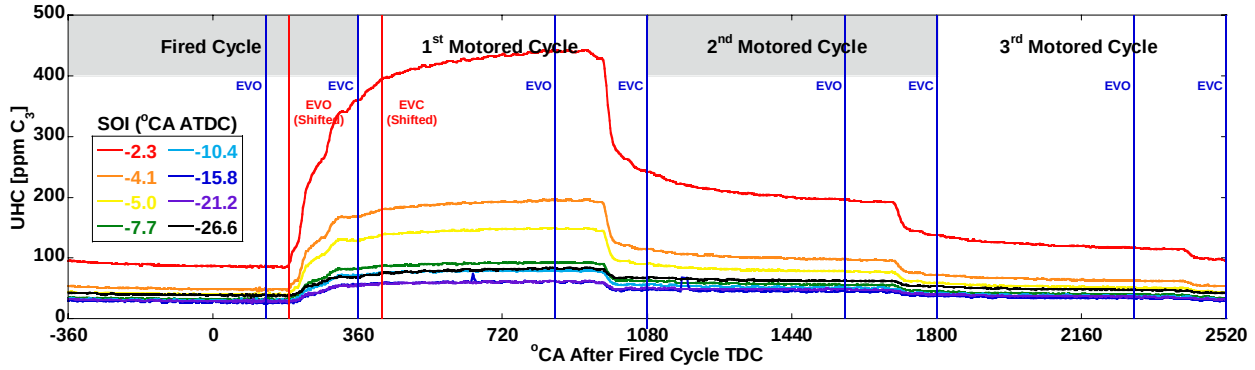

c)

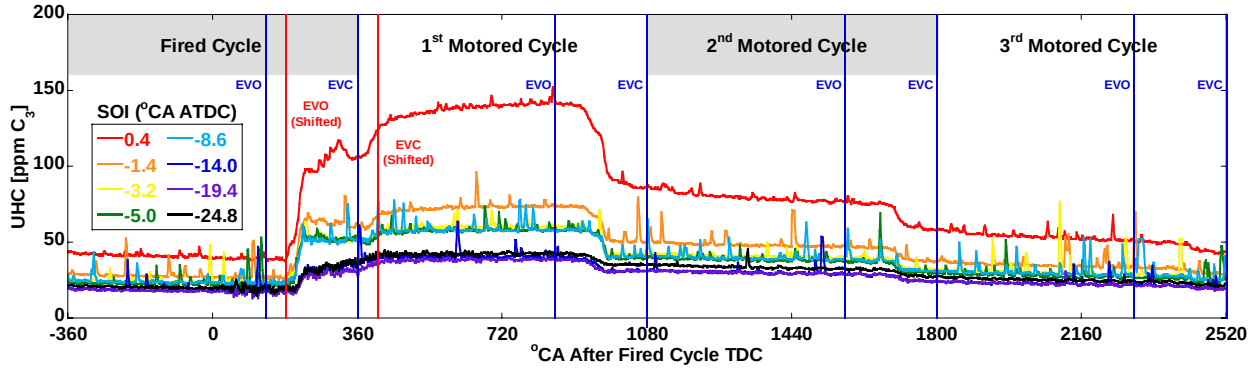

d)

Figure 12. Average UHC fast-FID traces shown for the entire skip-fired cycle for the (a) O_2 concentration sweep 3 bar load, (b) O_2 concentration sweep 8 bar load, (c) SOI sweep 3 bar load, and (d) SOI sweep 8 bar load. (note the scale is not the same for all plots)

A similar argument can also be made for the rapid increase in UHC concentration just prior to EVC for the 9% and 10% O_2 concentrations at 8 bar (Figure 13b) and the 8% O_2 concentration at 3 bar (Figure 13a, SOI = -29.3°CA for 8%). If fuel gets trapped in the squish volume, it could be quenched on either the piston top surface or the cylinder wall. As the piston rises during the exhaust stroke, UHC found in those quench layers would be forced out of the cylinder near EVC.

Another source of UHC includes contributions from the bulk gases. It is reasonable to assume that during the time of highest piston velocities, the exhaust is primarily composed of bulk gases. It is then possible to identify a region of interest (shown in Figures 13a-d) where the effect of bulk gases can be isolated.

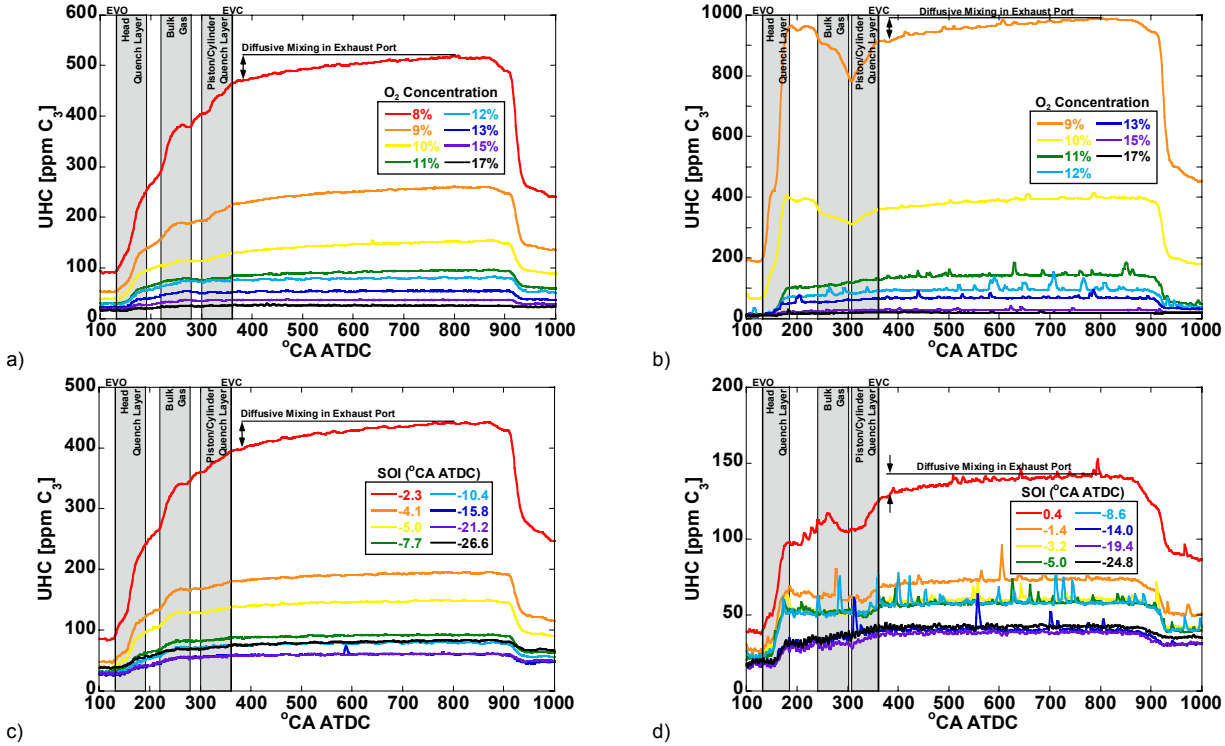

Figure 13.Interpretation of UHC fast-FID traces shown for fired cycle only for the (a) O_2 concentration sweep 3 bar load, (b) O_2 concentration sweep 8 bar load, (c) SOI sweep 3 bar load, and (d) SOI sweep 8 bar load. (note the scale is not the same for all plots)

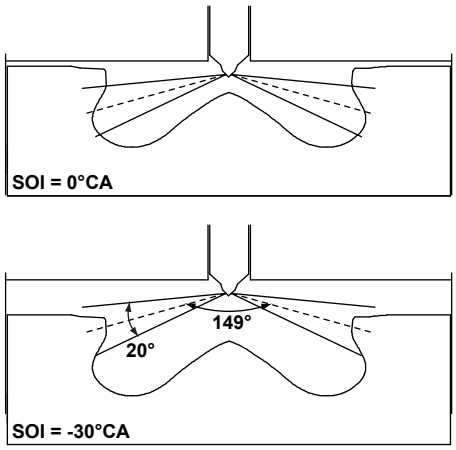

Figure 14. Schematic of fuel injection spray targeting at SOI = 0°CA and SOI = -30°CA.

Examining Figure 13a, the significance of UHC in the bulk gases increases with decreasing O_2 concentration at 3 bar load. One possibility for the increase in bulk gas UHC at low O_2 concentrations could be overmixing. As the ignition delay increases, more time is available for mixing, and a larger portion of the fuel may be found in mixtures which are too dilute to support complete combustion.

For the most retarded injection timings investigated in the SOI sweeps, it is expected that bulk gas quenching could begin to contribute to UHC as the ignition delay starts to rise. The highest UHC levels for the SOI sweeps occurred at the most retarded SOI cases, which also have the latest 50% burn angles (CA50 = 21.9°CA for SOI = 0.4°CA at 8 bar). The intermediate peak observed at 8 bar in Figure 13d for SOI = 0.4°, near 270°CA, is suggestive of bulk gas quenching contributions to UHC. Similarly, the bump in the 'bulk gas' region in Figure 13c increases with retarded SOI, also an indication of significant bulk gas quenching contributions to UHC.

Finally, it is useful to examine the UHC level activity after EVC. A steady rise in UHC concentration suggests diffusive mixing in the exhaust port after EVC. The change in UHC level from EVC to the peak (shown in Figures 13a-d) could therefore indicate the significance of the last UHC emitted prior to EVC.

Mass flow rate analysis of UHC

Looking at only the UHC concentrations could be misleading in some cases. For instance if a high UHC concentration occurred during a period of low exhaust mass flow then the impact of that source on the total UHC emissions would be low. To gain a better understanding of the relative impact of the different sources of UHC, the instantaneous FID signal is taken, along with the predicted instantaneous mass flow rate through the exhaust valves, to compute the UHC mass emissions on an intra-cycle basis.

This process is illustrated in Figure 15, which shows the fast-FID signal and the predicted exhaust mass flow rate from WAVE for the 10% O_2, 3 bar load case. Figure 15 also shows the EVO and EVC timing, corresponding to 0.15 mm valve-lift. There are two distinct periods that characterize the exhaust process. The first is the blowdown period, caused by the rapid exit of exhaust gases due to high cylinder pressure shortly after EVO. The second period occurs as piston motion forces the remaining gases out of the cylinder. There is also a brief flow reversal period between the blowdown period and exhaust stroke phase. The reversal is not shown on Figure 15 because the scale has been clipped at zero.

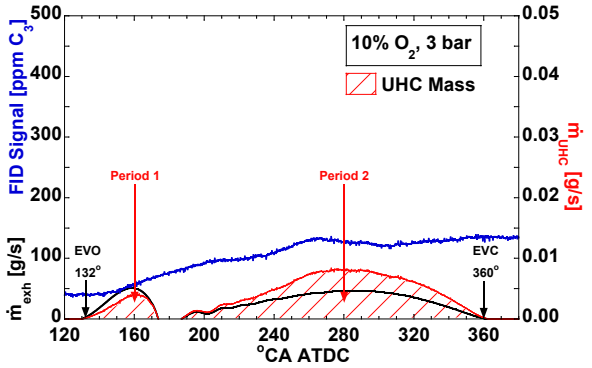

Figure 15. Representative single cycle FID trace for a 10% [O_2], 3 bar load condition showing the corresponding exhaust flow rate and resulting flow rate of UHC.

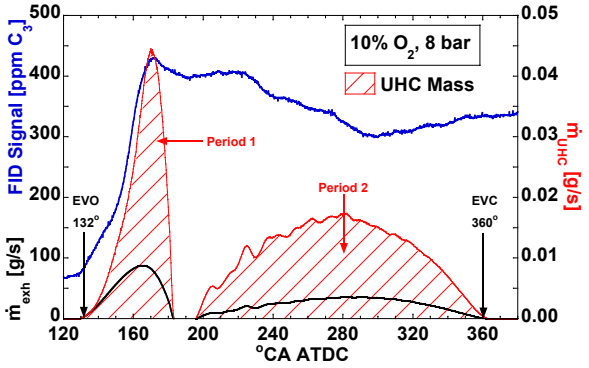

Figure 16. Representative single cycle FID trace for a 10% [O_2], 8 bar load condition showing the corresponding exhaust flow rate and resulting flow rate of UHC.

After converting the FID signal to an instantaneous mass fraction of UHC based on the emissions analysis, the curves were multiplied to generate the time-resolved mass flow rate of UHC, shown by the red shaded region in Figure 15. The exhaust flow rate of UHC was taken to be zero during the flow reversal period, although it is reasonable to assume that some UHC are drawn back into the cylinder during this time. The FID signal shown in Figure 15 has been advanced by 59°CA to match the signal phasing with EVO. The correct crank angle shift was determined by matching the initial rise in FID signal to the beginning of the exhaust process. A 59°CA shift was applied to all cases at the 3 bar load condition, while a smaller correction of 52°CA fit the measurements more closely for the 8 bar load condition.

The resulting mass flow rate of UHC shown in Figure 15, like the exhaust process, is separated into two distinct periods. The first period corresponds to the blowdown process and represents both the bulk gas UHCs and UHCs located within the firedeck quench layer. As discussed previously, it is believed that UHC stemming from the firedeck quench layer becomes much more prominent for early SOI. The second period corresponds to the expulsion of the remaining gases from the cylinder during the exhaust stroke. This second period will also have bulk gas contributions, but will additionally include other sources of UHC such as UHC present in the cool boundary layers near the cylinder wall and piston top, exiting towards the end of the exhaust stroke.

The same analysis is shown in Figure 16 for the 10% O_2, 8 bar load case, a condition for which a spike in UHC concentration was observed just after EVO, thought to be a result of spray targeting into the squish region. The 8 bar load also has a higher exhaust mass flow rate during the blowdown than the 3 bar load, because cylinder pressure at EVO is higher. By only comparing the raw FID signals of the 3 and 8 bar loads during the blowdown period shown in Figures 15 and 16, the impact of differences observed during this period on total UHC emissions would have been underestimated. Because of the higher blowdown mass flow rate at high loads, the high UHC concentration during blowdown is even more significant. Conversely, during the second period, there is a lower exhaust mass flow rate for a shorter duration at high load. The lower exhaust mass expelled lessens the impact of high UHC concentrations observed at high load during period 2.

Integration of both the UHC and exhaust mass flow rates over each period and dividing yields the mass fraction of UHC. As the exhaust mass flow rate distributions are primarily a function of cylinder pressure at EVO, they remain fairly constant at each load regardless of O_2 or SOI. This makes the UHC mass fractions a good indicator of how the UHC mass changes in periods 1 and 2 with O_2 and SOI.

The breakdown of UHC mass fractions is shown in Figures 17 and 18 for the O_2 sweeps at the 3 and 8 bar loads respectively. UHC COVs are also shown in Figures 17 and 18 and will be discussed in the following section. At low O_2 concentrations, and corresponding earlier injection timings, the mass fraction of period 2 rises faster than the mass fraction of period 1 for both loads. This might suggest that as more fuel is trapped within the squish region, the dominant source of UHC would be from the cylinder wall and piston top boundary layers, rather than from a quenched gas layer on the head. It is not possible to quantitatively separate the bulk gas UHC contributions to each period from crevice and quench layer contributions. However, we believe that the mass fraction of bulk gas UHC should be fairly constant between periods 1 and 2, even though the FID traces of UHC suggest that bulk gas UHC are not insignificant. Therefore, differences between the UHC mass fractions of periods 1 and 2 likely stem from sources other than the bulk gas.

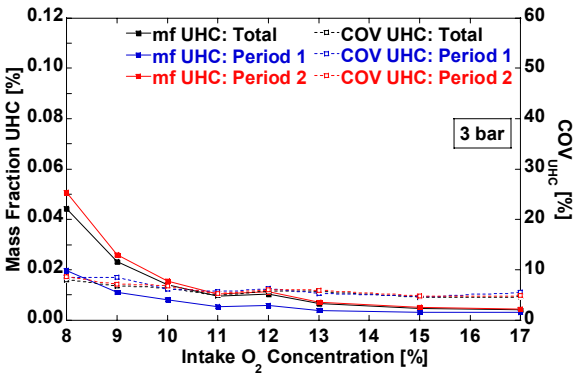

Figure 17. Distribution of UHC mass fractions and UHC COV for the 3 bar load condition as a function of O_2 concentration.

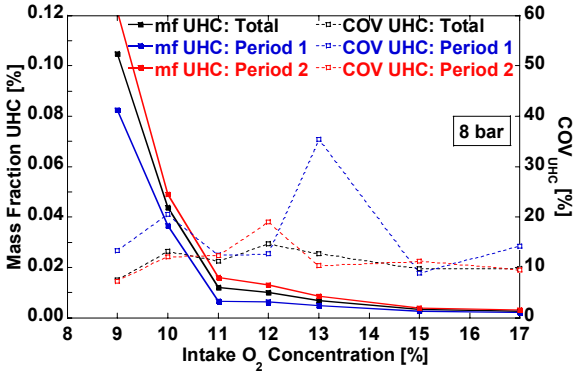

Figure 18. Distribution of UHC mass fractions and UHC COV for the 8 bar load condition as a function of O_2 concentration.

Calculated UHC mass fractions for the SOI sweeps are shown in Figures 19 and 20 for the 3 and 8 bar loads, respectively. At low load, the mass fraction of UHC in period 2 increases with respect to period 1 for retarded SOI (58% higher at earliest SOI, 136% higher at most retarded SOI). This is contrasted by the high load shown in Figure 20 where the relative mass fraction during period 2 is roughly 30-50% higher than period 1, regardless of SOI. Because the mass fraction of bulk gas UHC is assumed to remain constant between periods 1 and 2, this suggests that there is a significant increase in UHC from piston boundary layers and crevice volume sources at low load and retarded injection. The cycle-averaged emissions discussed above indicated that at low load, UHC oxidation was likely rate-limited by chemical kinetics. The increased importance of UHCs from cool boundary layer and crevice sources reinforces this previous observation.

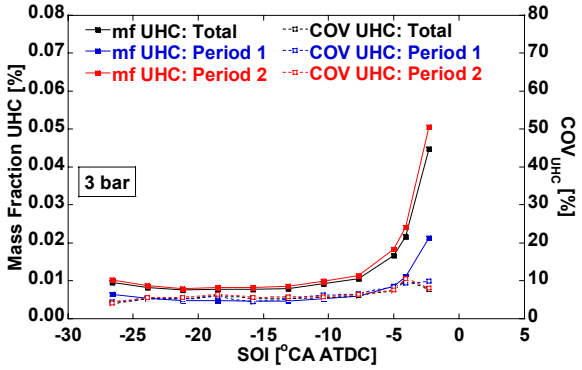

Figure 19. Distribution of UHC mass fractions and UHC COV for the 3 bar load condition as a function of SOI.

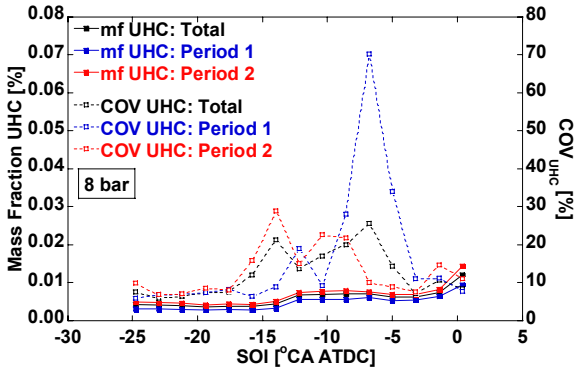

Figure 20. Distribution of UHC mass fractions and UHC COV for the 8 bar load condition as a function of SOI.

CYCLIC VARIABILITY IN UHC EMISSIONS

A central motivation for this work was to discover if increases in UHC emissions at low O_2 concentration and/or retarded SOI were caused by a deterioration of the mean cycle UHC levels, or if the increases were due to individual cycles with high UHC emissions. In general, increases in UHC emissions at low O_2 concentrations and retarded SOI did not correspond to significant increases in UHC COV, as shown for all cases in Figures 17 through 20. There are a few cases, however, for which the COV was significantly higher for either period 1 or period 2, most notably at high load.

Upon closer examination, in each case the high COV values were caused by a single 'bad' cycle out of the 75 fired cycles. One would expect the cycles with uncharacteristically high UHC emissions to have a corresponding low value of IMEP. However, that was not the case, as the cycles which caused high UHC COV values did not have a noticeably lower IMEP.

Figure 21 shows the FID signal and UHC mass flow rate for the cycle responsible for the high COV at 13% O_2 8 bar load shown in Figure 18. Noticeably, there is a spike in the FID signal during period 1. The source of the instantaneous spike in UHC is not definitively known. It could be due to one of a number of sources, including a packet of unburned liquid fuel, a deposit breaking loose from inside either the exhaust port or the FID probe, or impurities in the FID air or H_2 supplies. The significant observation, however, is that the spike in UHC signal did not noticeably affect the IMEP, or the mean UHC emissions at the 13% O_2 8 bar load condition.

High values of COV also occurred during period 2. Figure 22 shows the FID signal and UHC mass flow rate for one such occurrence at SOI = 14.0°CA and 8 bar load (shown in Figure 20, COV = 29% during period 2). Again, the crank-angle resolved emissions show an anomalous spike in UHC, which affects neither the IMEP nor the mean UHC emissions level.

Disregarding the individual cycles with the 'spikes' in FID signal causes outlying COV values to return to values consistent with the rest of the data. Accordingly, COV levels in both periods 1 and 2 change little as either O_2 concentration or SOI are

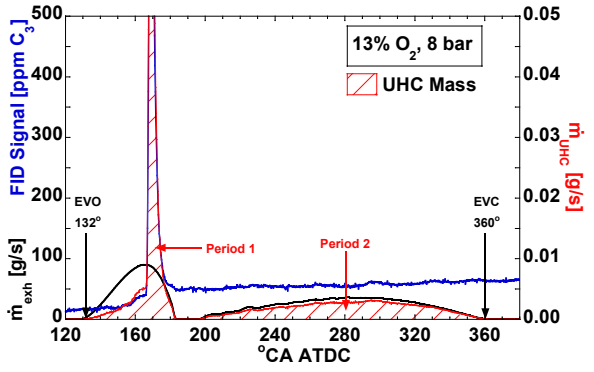

Figure 21. FID trace for the single 'bad' cycle at the 13% [O2], 8 bar load condition showing the corresponding exhaust flow rate and resulting UHC flow rate.

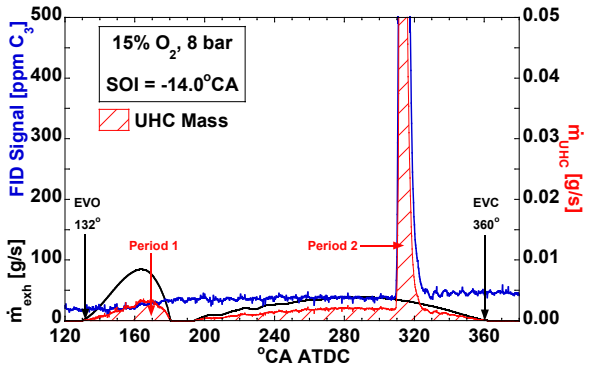

Figure 22. FID trace for the single 'bad' cycle at the 15% [O2], SOI = -14.0°CA, 8 bar load condition showing the corresponding exhaust flow rate and resulting UHC flow rate.

varied. Increases in UHC emissions are not accompanied by increases in COV, indicating that increases in UHC emissions stem from changing mean-cycle behavior, not isolated cycles that contribute disproportionately to the overall emissions. Overall, UHC cyclic variability measured in this study was at or below 10%. Compared to the cycle-to-cycle variability of other diesel emissions as reported by Zarling et al. [14], which place NO_x at 6% and particulates at nearly 40%, UHC emissions are at the lower end of the spectrum in terms of cycle-to-cycle variability.

SUMMARY AND CONCLUSIONS

Cycle- and crank-angle-resolved UHC emissions obtained with a fast-FID are examined in both high-dilution and late-injection LTC regimes—where simultaneously low NO_x and particulate emissions are countered by rapidly increasing CO and UHC emissions. Cycle-averaged emissions measurements of CO, NO_x, and soot are also presented. Load conditions of 3 and 8 bar IMEP are investigated.

Cycle-averaged emissions measurements revealed the expected trends:

- Increasing levels of UHC and CO at low O_2 concentrations or retarded SOI, with corresponding decreasing combustion efficiency.
- A characteristic soot 'hump' observed in both O_2 and SOI sweeps.
- Ultra-low NO_x levels for high-dilution, low O_2 concentration operation and acceptable NO_x emissions at retarded injection timing.

Fast FID traces of UHC emissions at high load show that at early SOI and high load there is a sharp spike in UHC concentration just after EVO. The UHC spike is possibly due to fuel injected directly into the squish volume and trapped in quench layers on the head and near the valve seats, which is expelled immediately after EVO. Under the same operating conditions, there is a rapid increase in UHC just before EVC. Potentially, this increase is also due to fuel injected into the squish volume, which persists in layers along the cylinder walls and piston top. Raw fast-FID traces also show significant UHC can be found in the bulk gases, resulting from both overmixing and bulk gas quenching.

The crank-angle resolved UHC mass fractions are also weighted by model predictions of the exhaust gas mass flow rate to examine the relative contributions to the UHC mass emissions. The results indicate that emissions stemming from cylinder and/or piston wall quench layers under early injection conditions may dominate over emissions trapped in quench layers on the head surface. At light load and retarded injection, emissions stemming from cool cylinder and/or piston wall layers are of increasing importance. This is consistent with the cycle-averaged emissions results, which suggest that under these conditions HC oxidation is limited by finite-rate kinetics, rather than insufficient mixing.

The COV values of UHC emissions were found to be approximately constant, even at highly-dilute or retarded-injection conditions when UHC emissions increased rapidly. This suggests that the increase in UHC levels is predominantly a result of increases in the mean cycle behavior. Engine simulation codes that correctly capture the mean cycle behavior will thus be sufficient to identify and minimize the sources of these emissions.

ACKNOWLEDGMENTS

Support for this research was provided by the U.S. Department of Energy, Office of FreedomCAR and Vehicle Technologies. The research was performed at the Combustion Research Facility, Sandia National Laboratories, Livermore, California. Sandia is a multiprogram laboratory operated by Sandia Corporation, a Lockheed Martin Company, for the United States Department of Energy's National Nuclear Security Administration under contract DE-AC04-94AL85000. The authors are grateful to General Motors for providing the engine head, as well as for their input into the project. The authors are also grateful to Kenneth St. Hilaire and Lloyd Claytor of Sandia National Laboratories for their assistance with the fast FID probe setup.

REFERENCES

1. Heywood, J. B., Internal Combustion Fundamentals, McGraw-Hill, Inc., New York, 1988.
2. Finlay, I. C., Boam, D. J., Bingham, J. F. and Clark, T. A. "Fast Response FID Measurement of Unburned Hydrocarbons in the Exhaust Port of a Firing Gasoline Engine," SAE paper 902165, 1990.
3. Jensen, T. K., Schramm, J., Narusawa, K. and Hori, S. "Analysis of UHC Emission from a Natural Gas SI Engine Using Fast Response FID and a Heat Release Model," SAE paper 2001-01-3533, 2001.
4. Tabaczynski, R. J., Heywood, J. B. and Keck, J. C., "Time-Resolved Measurements of Hydrocarbon Mass Flow Rate in the Exhaust of a Spark-Ignition Engine," SAE paper 720112, *SAE Transactions*, v. 81, pp. 379-391, 1972.

5. Marriott, C. D., Kong, S.-C. and Reitz, R. D., "Investigation of Hydrocarbon Emissions from a Direct Injection-Gasoline Premixed Charge Compression-Ignited Engine," SAE paper 2002-01-0419, *SAE Transactions*, v. 111, 2002.
6. Schurov, S., Collings, N., Hands, T., Peckham, M. and Burrell, J. "Fast Response NO/HC Measurements in the Cylinder and Exhaust Port of a DI Diesel Engine," SAE paper 980788, 1998.
7. Kook, S., Bae, C., Miles, P. C., Choi, D. and Pickett, L. M., "The Influence of Charge Dilution and Injection Timing on Low-Temperature Diesel Combustion and Emissions," SAE paper 2005-01-3837, *SAE Transactions*, v. 114, 2005.
8. Silvis, W. M. "An Algorithm for Calculating the Air/Fuel Ratio from Exhaust Emissions," SAE paper 970514, 1997.
9. Akihama, K., Takatori, Y., Inagaki, K., Sasaki, S. and Dean, A. M., "Mechanism of the Smokeless Rich Diesel Combustion by Reducing Temperature," SAE paper 2001-01-0655, *SAE Transactions*, v. 110, 2001.
10. Noehre, C., Andersson, M., Johansson, B. and Hultqvist, A. "Characterization of Partially Premixed Combustion," SAE paper 2006-01-3412, 2006.
11. Ogawa, H., Li, T., Miyamoto, N., Kido, S. and Shimizu, H. "Dependence of Ultra-High EGR and Low Temperature Diesel Combustion on Fuel Injection Conditions and Compression Ratio," SAE paper 2006-01-3386, 2006.
12. Kimura, S., Aoki, O., Ogawa, H., Muranaka, S. and Enomoto, Y., "New Combustion Concept for Ultra-Clean and High-Efficiency Small DI Diesel Engines," SAE paper 1999-01-3681, *SAE Transactions*, v. 108, 1999.
13. Naber, J. D. and Siebers, D. L., "Effects of Gas Density and Vaporization on Penetration and Dispersion of Diesel Sprays," SAE paper 960034, *SAE Transactions*, v. 105, 1996.
14. Zarling, D. D., Pipho, M. J. and Kittelson, D. B., "Measurement of Cyclic Variability in a Diesel Engine Using a Single Cycle Sampler," SAE paper 930602, *SAE Transactions*, v. 102, 1993.

CONTACT

Will Colban: Combustion Research Facility, Sandia National Laboratories, MS 9053, P.O. Box 969, Livermore, CA 94551-0969, Phone: (925)-294-2621, Fax: (925)-294-1004, Email: wcolban@sandia.gov.

DEFINITIONS, ACRONYMS, ABBREVIATIONS

AHRR: Apparent Heat Release Rate
ATDC: After Top Dead Center
BA: Burn Angle
CA: Crank Angle
CO: Carbon Monoxide
CO_2: Carbon Dioxide
COV: Coefficient of Variation
CR: Compression Ratio
DI: Direct Injection
EGR: Exhaust Gas Recirculation
EVC: Exhaust Valve Closing
EVO: Exhaust Valve Opening
FID: Flame Ionization Detector
FSN: Filter Smoke Number
HC: Hydrocarbons
IMEP: Indicated Mean Effective Pressure
IVC: Intake Valve Closing
IVO: Intake Valve Opening
$\dot{m}_{exh}$: Predicted Exhaust Mass Flow Rate
$\dot{m}_{UHC}$: Mass Flow Rate of UHC
MBT: Maximum Brake Torque
MK: Modulated Kinetics
NO_x: Nitrogen Oxides
RPM: Rotations per Minute
SI: Spark Ignition
SOI: Start of Injection
TDC: Top Dead Center
T_{in}: Intake Temperature
UHC: Unburned Hydrocarbons
η_c: Combustion Efficiency
ϕ_{avg}: Average In-Cylinder Equivalence Ratio